Conf-940548--7

NREL/TP-441-7080 • UC Category: 1213 • DE94011865

Evidence that Aerodynamic Effects, including Dynamic Stall, Dictate HAWT Structure Loads and Power Generation in Highly Transient Time Frames

Marvin W. Luttges
Mark S. Miller
Michael C. Robinson
Derek E. Shipley
David A. Simms

Prepared for
Windpower '94
May 9-13, 1994
Minneapolis, Minnesota

National Renewable Energy Laboratory
1617 Cole Boulevard
Golden, Colorado 80401-3393
A national laboratory of the U.S. Department of Energy
Managed by Midwest Research Institute
for the U.S. Department of Energy
under contract No. DE-AC36-83CH10093

Prepared under Task No. WE418120

August 1994

NOTICE

Available to DOE and DOE contractors from:
Office of Scientific and Technical Information (OSTI)
P.O. Box 62
Oak Ridge, TN 37831
Prices available by calling (615) 576-8401

Available to the public from:
National Technical Information Service (NTIS)
U.S. Department of Commerce
5285 Port Royal Road
Springfield, VA 22161
(703) 487-4650

Printed on paper containing at least 50% wastepaper and 10% postconsumer waste

EVIDENCE THAT AERODYNAMIC EFFECTS, INCLUDING DYNAMIC STALL, DICTATE HAWT STRUCTURAL LOADS AND POWER GENERATION IN HIGHLY TRANSIENT TIME FRAMES

Derek E. Shipley, Mark S. Miller, Michael C. Robinson, Marvin W. Luttges
Department of Aerospace Engineering Sciences
University of Colorado, Boulder, CO 80309
and
David A. Simms
National Renewable Energy Laboratory, Golden, CO 80401

ABSTRACT

Aerodynamic data collected from the National Renewable Energy Laboratory's Combined Experiment have shown three distinct performance regimes when the turbine is operated under relatively steady flow conditions. Operating at blade angles of attack below static stall, excellent agreement is achieved with two-dimensional wind tunnel data. Around the static stall angle, the cycle average normal force produced is greater than the static test data. Span locations near the hub produce extremely large values of normal force coefficient, well in excess of the two-dimensional data results. These performance regimes have been shown to be a function of the three-dimensional flow structure and cycle averaged dynamic stall effects. Power generation and root bending moments have also been shown to be directly dependent on the inflow wind velocity. Aerodynamic data, including episodes of dynamic stall, have been correlated on a cycle by cycle basis with the structural and power generation characteristics of a horizontal axis wind turbine. Instantaneous unsteady forces and resultant power generation indicate that peak transient levels can significantly exceed cycle averaged values. Strong coupling between transient aerodynamic and resonant response of the turbine was also observed. These results provide some initial insight into the contribution of unsteady aerodynamics on undesirable turbine structural response and fatigue life.

INTRODUCTION

Wind turbine blade failure and the subsequent costs due to repair, replacement, and turbine downtime are a severe problem for the wind turbine industry. For known blade problems alone, repair and replacement costs are estimated at $40-60 million (Lynette 1989). Blade failure can primarily be attributed to inadequate knowledge of the aerodynamic loads a blade experiences in the field. Since rotor loads are carried through the entire system, a more complete understanding of the aerodynamic inputs and their affects on the various structural components would allow turbine and blade designers to create more durable, efficient, and cost effective designs.

The structural loading and power generation of a horizontal axis wind turbine (HAWT) are influenced by a variety of forces including: centrifugal, inertial, gravitational, and aerodynamic. Of these, the aerodynamic forces are least understood. Horizontal and vertical axis wind turbines operating in the field experience one of the most complex flow environments encountered by any

aerodynamic device. HAWT geometries provide highly three-dimensional flows with strong radial (spanwise) pressure and velocity gradients. Highly variable wind conditions can produce major alterations in both inlet flow magnitude and direction. These alterations in the inlet behavior may be further complicated by the addition of other large flow disturbances introduced from turbines operating upwind as is typical in wind farms.

This combination of turbine geometry and turbulent inflow varies the localized turbine blade velocity field along the span, simultaneously producing blade operating environments ranging from fully stalled to fully attached flow. The rapidly changing inlet flow conditions can dynamically drive flow separation and create extremely large, non-linear, transient loading along the blade span. These loads are propagated throughout the wind turbine. As a result, the turbine experiences significant fatigue which shortens the operational life and increases maintenance.

The present investigation focuses on the aerodynamic forces which drive power generation and structural loading of the turbine. Although aerodynamic effects are the prime contributor, other factors play a significant role. Understanding the relationship between aerodynamics, power generation, and structural loading provides some insight into the complex dynamic response of horizontal wind turbines.

TEST SET-UP

Unsteady aerodynamic, structural, and turbine performance data have been collected using the National Renewable Energy Laboratory's (NREL's) Combined Experiment horizontal axis wind turbine (Butterfield et al, 1992). The wind turbine (Figure 1) is a 10.1 m (33.1 ft) diameter, three-bladed machine that rotates at a constant 72 RPM and is capable of producing 20 kW of power. The turbine is supported on a 0.4 m (1.3 ft) cylindrical column at a height of 17 m (55.8 ft) from the ground to the center of the hub. The blades used were rectangular, untwisted NREL S809 airfoil sections with a 45.7 cm (18 in) chord. One of the three blades was completely instrumented with pressure transducers (Figure 2) at four different span locations. Unsteady pressure data from all transducers was collected simultaneously. The data sample rate, 521 Hz, was sufficient to capture the dynamic and transient pressure events elicited from time variant inlet flow conditions.

The inlet flow conditions were measured by the Vertical Plane Array located 12 m (39.4 ft) upwind of the turbine. The inlet flow magnitude and direction across the turbine diameter were measured using 11 prop-vane and 2 bi-vane anemometers. Eight of the prop-vane anemometers were arranged in a 4 m (13.1 ft) radius circle approximately 16 m (52.5 ft) above the ground. The remaining anemometers were spaced evenly inside the circle in a vertical line. The two bi-vane anemometers were mounted outside the circle on the horizontal axis.

Strain gages mounted on the blades and low-speed shaft were used to measure the rotor's mechanical loads. Torsional and edgewise bending moments were measured at the root of the instrumented blade and at two spanwise locations. Flapwise bending moments were measured at the roots of all three blades and at five spanwise locations on the instrumented blade (Figure 2). Mechanical turbine power is determined from measured low-speed shaft torque and rotor

speed. Electrical power is measured via a power watt transducer connected to the 3-phase, 480 VAC induction generator.

Data was collected over a wide range of nominal operating conditions for the turbine. Each data run consisted of a five minute continuous data collection episode wherein all data was stored on time encoded tape. The turbine blades rotated at a constant 1.2 Hz, thus, approximately 360 consecutive blade rotation cycles are contained in each 5 minute episode. A total of 59 episodes were collected representing 21,000 complete rotational cycles of the instrumented turbine blade. The total 59 tape data set consists of 9 Gbytes of data and requires 30 optical disks for storage.

RESULTS & DISCUSSION

The local blade angle of attack along the span was the major determinant of airfoil aerodynamic performance The angle of attack (α) is a product of three variables: inlet flow velocity (Vw), blade rotational velocity at that span location ($r\omega$), and yaw angle (γ) of the turbine disk relative to the inflow (Figure 3). Any change in these variables alters the local angle of attack and changes the blade's aerodynamic response.

The influence of inflow and rotational velocity is shown in Figure 4. Angle of attack increases with wind velocity and decreases with span location. Operation at yaw angles other than 0° induces cyclic variations in the wind velocity relative to the blade, and hence in angle of attack (Figure 5). The azimuth angle (ψ) indicates the location of the instrumented blade as it rotates from zero degrees (blade straight up).

Previous investigation by these authors established an aerodynamic performance baseline for 0° yaw (Robinson et al 1993, Robinson et al 1994, and Young 1993). Using this baseline, three operational performance regimes were found based upon angle of attack (Figure 6). This figure shows the cycle averaged normal force coefficient, Cn, as a function of the cycle averaged angle of attack. The first regime occurs below static stall (less than 17°) where Cn shows excellent agreement with two-dimensional wind tunnel data. The second regime is at angles greater than static stall and includes the outer three span locations. Within this region the cycle averaged Cn values remain level where the two-dimensional wind tunnel data decreases due to stall. The third regime occurs at angles greater than static stall and includes only the 30% span location. In this region extremely large values of Cn are produced, well in excess of two-dimensional results. Similar results for other turbines have been obtained by Madsen (1991) and Ronsten et al (1989). These performance regimes have been shown to be a function of the three-dimensional flow structure and dynamic stall effects (Robinson et al 1993 and Robinson et al 1994).

The current study extended the previous results to include yaw angles of -20°, -10°, 10°, and 20° for all four span locations. The 0° yaw baseline was created by averaging data from three consecutive cycles that exhibited approximately the same velocity at roughly 0° yaw. However, due to the tendency of a downwind HAWT to self-align with the local flow direction, it was not possible to compile a large enough sample set at yaw angles other than 0° using three cycle groupings. Therefore, all baseline data sets were constructed by cycle averaging single cycles that exhibited constant inflow conditions. These data sets, for all four span locations, are co-plotted with the 0° yaw baseline in Figure 7.

All five yaw angle conditions reduce on the local angle of attack; however, the variance is greater than the 0° yaw condition. The variance increases significantly at higher yaw angles. This effect is caused by the large change in α over a cycle at high yaw (Figure 5). Despite the increased variance, there are no significant deviations from the performance trends of the 0° yaw condition reported earlier.

CYCLE AVERAGED

The influence of aerodynamic forces on structural loading was obtained from a simple analytic model which estimates the root bending moments from the normal and tangential aerodynamic force values. The blade was divided into four sections each encompassing one of the four primary pressure tap locations (30%, 47%, 63%, and 80% span). Aerodynamic force measurements, Cn and Ct, taken at the four span locations were multiplied by the section area, A_i, and the dynamic pressure, q_i, to obtain the average force over each blade section (Figure 8). Thus, the bending moments due to aerodynamic forces in the normal and tangential directions are the sum of the forces multiplied by their respective moment arms, r_i.

The model included a constant centrifugal force term to account for blade coning. The moment due to centrifugal forces is given by $M_c = mr_{cg}^2\Omega^2\sin\phi$ where m equals the mass of the blade, r_{cg} equals the radial distance to the blades's center of gravity, Ω equals the rotational frequency, and ϕ is equal to the coning angle. Then, the moment in the flap direction is $M_{flap} = M_{aero,flap} - M_c\sin(\beta)$ and the moment in the edge direction is $M_{edge} = M_{aero,edge} + M_c\cos(\beta)$ where β is the blade pitch angle. Thus, M_{flap} is in the normal direction and M_{edge} is in the tangent direction.

Figures 9 and 10 compare the measured and calculated root flap and edge bending moments. In both cases, agreement between the calculated and measured values is excellent, particularly at low velocities. At higher velocities the moment calculated from aerodynamic data overpredicts measured flap bending and underpredicts edge bending. Overall, mean flap and edge bending moments over a cycle can be calculated from the aerodynamic force data directly. Also, the cycle averaged bending moments do not appear to depend upon yaw since all yaw conditions collapse on wind velocity.

An estimate of the torque applied to the generator (low speed) shaft was made from the calculated aerodynamic moments in the plane of rotation (Figure 8). Pressure data was available for only a single blade, hence, the single blade torque value was multiplied by a factor of three to estimate the cycle averaged aerodynamic forces from all three blades. A comparison between the calculated shaft torque and measured low speed shaft torque is given in Figure 11 for all five yaw cases. The calculated and measured data correlate well at velocities below 17 m/s. At higher velocities measured shaft torque continues to increase while the calculated data levels off. This effect is due to the difference between calculated and measured edge bending at higher velocities as shown previously in Figure 10.

Generator power is a linear function of the low-speed shaft torque. Cycle averaged generator power for all five yaw cases is shown in Figure 12. It is clear that the measured data and the power calculated from aerodynamic forces correlate as expected. Also shown is estimated generator power based on predictions from the PROP computer code (Wilson et al 1976). Resulting mechanical power values from PROP are multiplied by an estimated generator

efficiency of 91% to provide comparable electrical power. PROP model results compare reasonably well with measured values at velocities below 17 m/s. The PROP power overpredictions of approximately 1 kW are most likely due to air density or pitch angle differences between the model inputs and turbine operating conditions. Above 17 m/s the PROP prediction and the measured data diverge, with measured generator power continuing to increase. This increase has been shown to be due to highly transient dynamic stall events and three-dimensional effects (Robinson et al 1993 and Robinson et al 1994) which increase power output beyond predicted values.

INSTANTANEOUS RESPONSE

Dynamic stall effects are not specifically evident in the data shown in Figures 9-12 because the cycle averaging process smooths out the transient dynamic stall excursions. Some indication of the increased dynamic loading is evident in the variance change of the mean "cycle averaged" data. For example, in Figure 13 the mean root flap bending moment is plotted with a 1σ deviation to show how the dynamic excursions dramatically increase at high velocities. Increased velocity produces larger local angle of attacks and an increase in the number of dynamic stall events.

Yawed turbine operation can induce dynamic stall at wind velocities which would otherwise not produce such effects (Figure 14). The highly transient dynamic stall event occurs at approximately 180° azimuth and affects 10% of the rotational cycle. Dynamic stall was triggered here by the excursion of the local blade angle below stall due to yaw and tower shadow. Although Cn values can exceed peak steady state wind tunnel values by 200% to 300%, they can easily be masked by averaging over an entire cycle. Structural loading and power generation deviations are obscured in a similar manner. It is clear that the influences of unsteady and three-dimensional aerodynamics are difficult to determine through cycle averaging data reduction methods alone. An instantaneous time history is also required.

To illustrate the effects of dynamic stall on structural loading and power generation, two rotation cycles were selected with significantly different aerodynamic conditions. Dynamic stall does not occur in the low velocity condition (8.08 $\pm$ 0.03 m/s, 0.47 $\pm$ 0.43° yaw). The 47% span upper surface pressure profile (Figure 15) indicates attached flow over the entire cycle. Only a pressure deficit from the tower shadow at 180° is evident. In contrast, the high inflow velocity case (15.72 $\pm$ 0.04 m/s, 5.06 $\pm$ 1.22° yaw) exhibits a large leading edge pressure peak indicative of dynamic stall (Figure 16).

Instantaneous root flap bending moments are plotted in Figure 17 for the low and high velocity cases. Also shown are the corresponding aerodynamic moments calculated using the force integration method previously discussed. Consistent with the cycle averaged data, the measured flap bending moments are well predicted by the aerodynamic data, especially for the low velocity case. The oscillations seen in root flap bending moment over the later half of both cases are due to blade resonance and cannot be predicted from the aerodynamics alone. Thus, it is clear that both aerodynamics and coupled blade dynamics play a major role in determining flap bending moment.

In both cases blade aerodynamic forces are significantly affected by the reduced velocity region behind the turbine tower. As the blade enters this region the angle of attack first decreases then rapidly increases during shadow exit. In the low velocity case (Figure 17), blade angle of attack does not exceed stall. This sudden impulse of the tower shadow excites the blade into oscillations at its fundamental frequency (4.8 Hz in the flapwise direction) of approximately 900 Nm peak-to-peak.

The same behavior can be seen in the high velocity case. However, the impulse provide by the tower shadow and dynamic stall is much greater. The corresponding resonance is 200% greater.

Instantaneous measured edge flap bending moments are plotted in Figure 18 for the low and high velocity cases. As before, the calculated aerodynamic moments are also plotted. In both cases the root edge bending moment is dominated by a sinusoidal wave caused by gravitational loading. The magnitude of the gravitational component in the edgewise direction varies sinusoidally with the maximum values occurring when the blade is horizontal, (90° and 270°). In comparison to the gravity effect, aerodynamics play only a small part in determining the instantaneous values.

Aerodynamics, however, play a large role in determining root edge resonance magnitude. As with flapwise bending, resonance is amplified by unsteady aerodynamic events. In the high velocity case, the fundamental frequency of the root edge bending moment (~7 Hz) is excited by dynamic stall. The magnitude of the resonance exceeds the low velocity case by more than 200%. The excitation is a result of the unique pressure field which occurs during the dynamic stall event. Rapid pressure decrease over the leading edge creates a negative drag component (thrust) on the turbine blade. This thrust excites the root edge bending moment. Resonance in the first half of the high velocity case is instigated by a large dynamic stall event that occurred in the previous cycle.

It is clear from these data that the previous load history directly affects the instantaneous load values due to resonance of the individual turbine blades. Aerodynamics must be coupled with the resonant history in order to adequately predict the resulting shaft torque. Due to the random variation between flow conditions on the three separate blades, simple assumptions that each blade produces similar cyclic responses are not correct. This result is highlighted in Figure 19. Here, the measured shaft torque is compared with torque calculated from the aerodynamic forces on the instrumented blade. The single blade result was phase shifted and added to reflect the contribution of the other two blades. The result correlates poorly with the actual measured value for both the low and high velocity case. Large peaks at high velocity reflect dynamic stall occurring on the instrumented blade.

CONCLUSIONS

These preliminary results highlight the importance of coupled transient loads analysis in predicting the load history and resulting fatigue life for horizontal axis wind turbines. Cycle averaged data provide adequate measures of steady state performance for blade aerodynamics, structural loading, and power generation. However, the large effects due to resonance of long slender blade sections are masked with this approach. Likewise, the transient impulse loads from dynamic stall events are not revealed. Instantaneous loads have been shown to be a complex

interaction between aerodynamics, resonance, load history, and coupled dynamic loading. Stochastic methods will probably be necessary to provide fatigue life cycle data for field operation environments.

REFERENCES

Butterfield, C.P., W.P. Musial, and D.A. Simms (1992): "Combined Experiment Phase I Final Report", TP-257-4655, NREL, Golden, CO.

Lynette, R. (1989): "California Wind Farms: Operational Data Collection and Analysis", SERI/PR-217-3489, NREL, Golden, CO.

Madsen, H.A. (1991): "Aerodynamics of a Horizontal-Axis Wind Turbine in Natural Conditions", Riso National Laboratory, Roskilde, Denmark, RISO-m-2903.

Robinson, M.C., M.W. Luttges, M.S. Miller, D.E. Shipley, and T.S. Young (1993): "Wind Turbine Blade Aerodynamics: The Combined Experiment", Windpower '93 Conference Proceedings, San Francisco, CA, July 12-16.

Robinson, M.C., M.W. Luttges, M.S. Miller, D.E. Shipley, and T.S. Young (1994): "Wind Turbine Blade Aerodynamics: The Analysis of Field Test Data", 13th ASME/ETCE Wind Energy Symposium Proceedings, New Orleans, LA, January 23-26.

Ronsten, G., J. Dahlberg, and S. Meijer (1989): "Pressure Measurements on a 5.35 m HAWT in CARDC 12 m X 16 m Wind Tunnel Compared to Theoretical Pressure Distributions", Proceedings of the European Wind Energy Conference, Glasgow, Scotland.

Wilson, R.E., P.B. Lissaman, and S.N. Walker (1976): "Aerodynamic Performance of Wind Turbines: Final Report", ERDA/NSF/04014-76/1, Department of Mechanical Engineering, Oregon State University, Corvallis, OR.

Young, T.S. (1993): "Using Digital Filtering Techniques as an Aid in Wind Turbine Data Analysis", Presented at the AIAA Region V Student Conference, Fort Collins, CO, April 21-24.

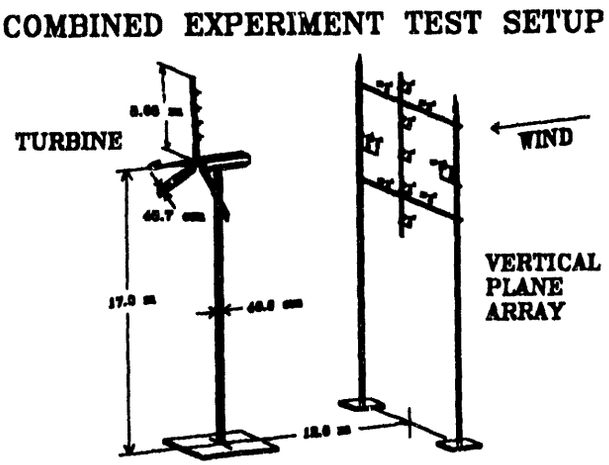

FIGURE 1: VIEW OF THE COMBINED EXPERIMENT TEST SITE INCLUDING THE GRUMMAN WIND STREAM 33 HORIZONTAL AXIS WIND TURBINE AND THE VERTICAL PLANE ARRAY.

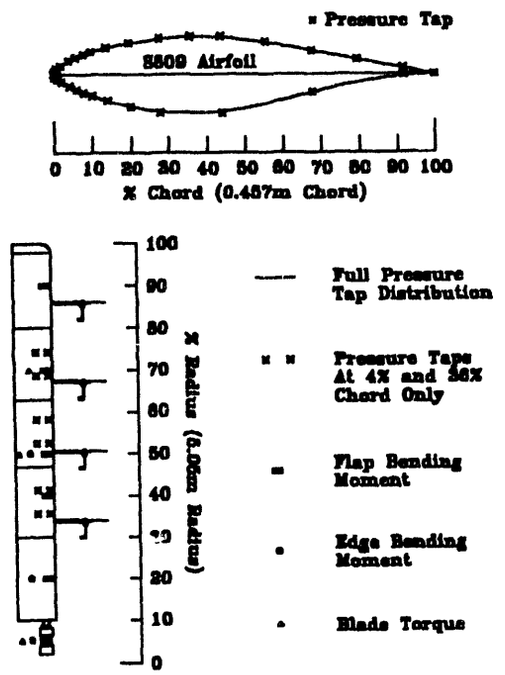

FIGURE 2: ROTOR BLADE CROSS SECTION AND LONGITUDINAL VIEWS SHOWING CHORDWISE PRESSURE TAP DISTRIBUTION AT EACH OF FOUR PRIMARY LOCATIONS (30%, 47%, 63%, AND 80% SPAN) AND LOCATION OF STRAIN GAGES.

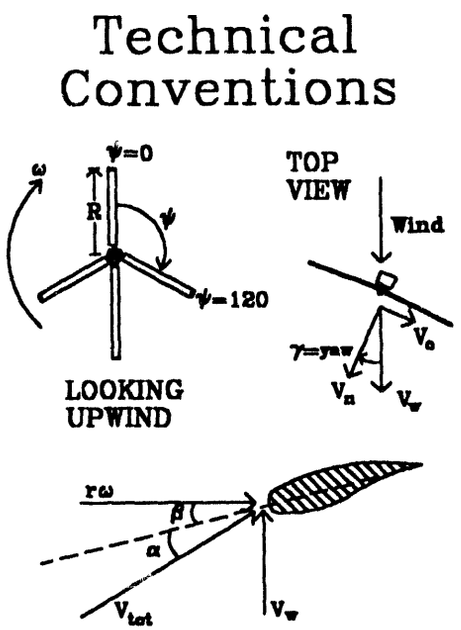

FIGURE 3: GEOMETRICAL RELATIONSHIPS BETWEEN INFLOW VARIABLES AND A DOWNWIND HORIZONTAL AXIS WIND TURBINE.

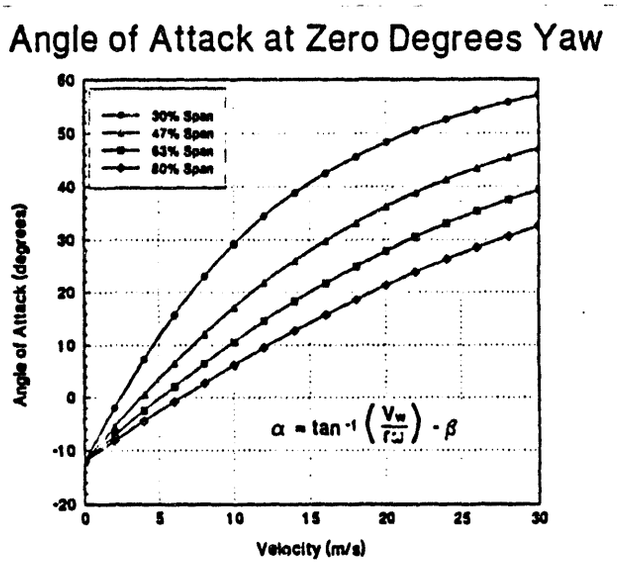

FIGURE 4: THEORETICAL ANGLE OF ATTACK BASED ON FREESTREAM VELOCITY AT ZERO DEGREES YAW FOR 30%, 47%, 63%, AND 80% SPAN.

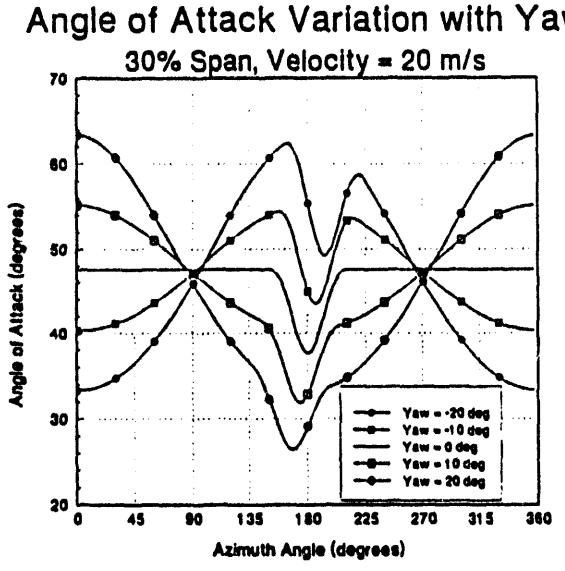

FIGURE 5: VARIATION OF ANGLE OF ATTACK OVER A ROTATIONAL CYCLE AT VARIOUS YAW ANGLES FOR 30% SPAN. THE EFFECT OF PASSAGE THROUGH THE TOWER SHADOW IS ALSO ILLUSTRATED.

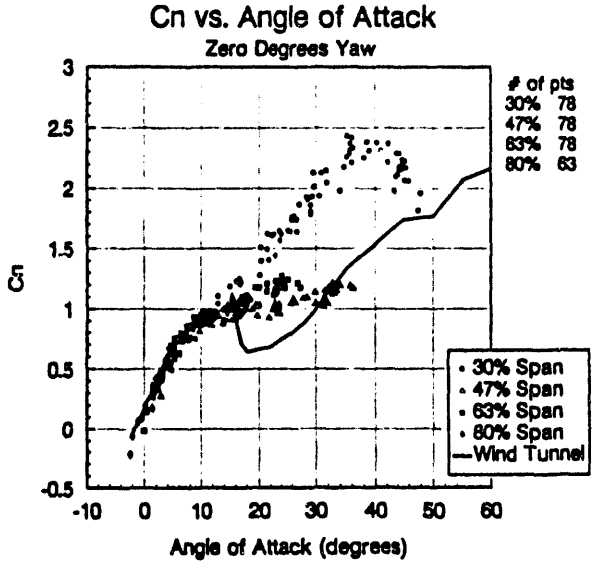

FIGURE 6: AERODYNAMIC PERFORMANCE BASELINE FOR ZERO DEGREES YAW SHOWING THE THREE PERFORMANCE REGIMES.

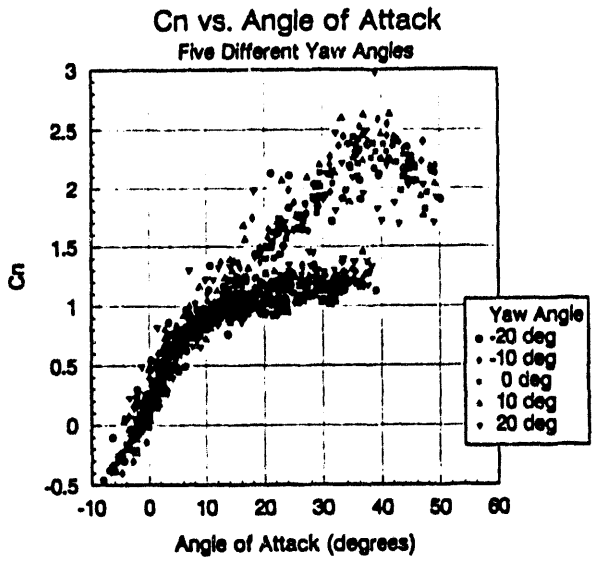

FIGURE 7: COMPARISON OF NORMAL FORCE COEFFICIENT AT FIVE DIFFERENT YAW ANGLES.

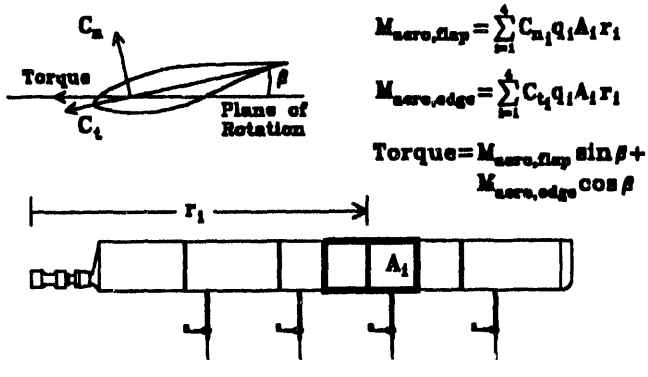

FIGURE 8: MODEL USED TO CALCULATE MOMENTS IN THE FLAP AND EDGE DIRECTION FROM AERODYNAMIC FORCE COEFFICIENTS. TORQUE IN THE PLANE OF ROTATION IS ALSO DEFINED.

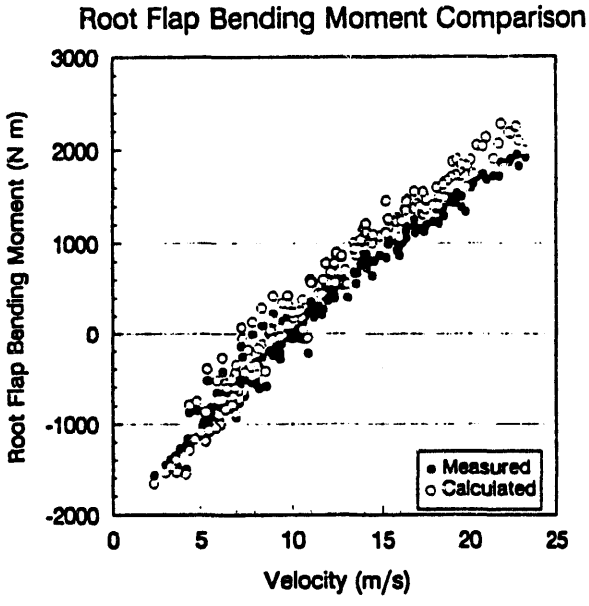

FIGURE 9: COMPARISON OF CYCLE AVERAGED MEASURED ROOT FLAP BENDING MOMENT TO FLAP MOMENT CALCULATED FROM NORMAL FORCE COEFFICIENTS

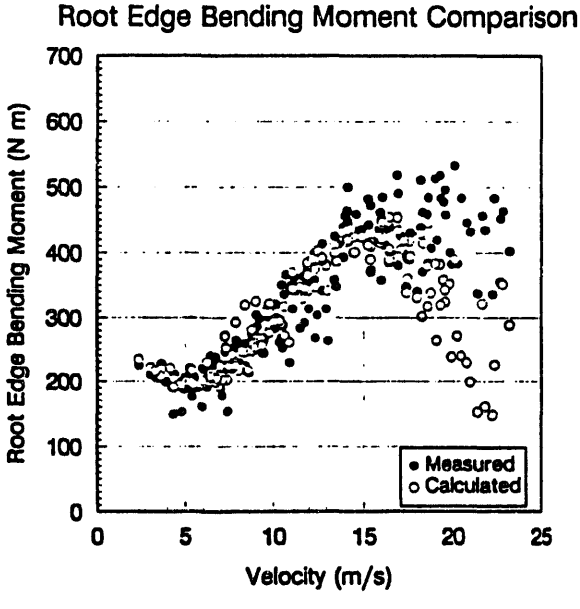

FIGURE 10: COMPARISON OF CYCLE AVERAGED ROOT EDGE BENDING MOMENT TO EDGE MOMENT CALCULATED FROM TANGENTIAL FORCE COEFFICIENT.

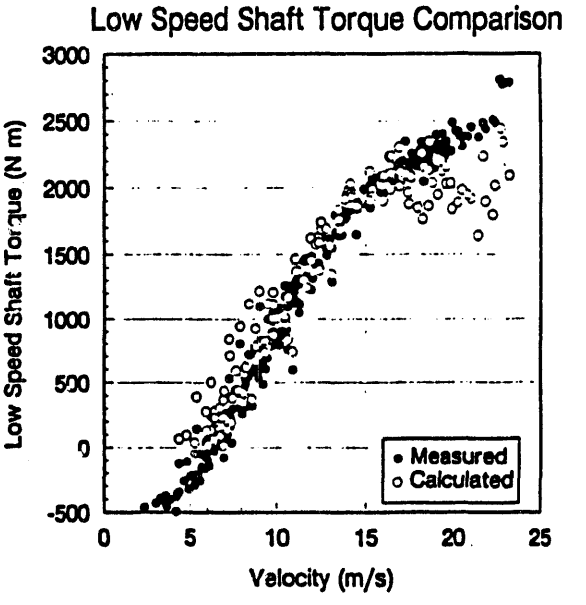

FIGURE 11: COMPARISON OF CYCLE AVERAGED LOW SPEED SHAFT TORQUE TO SHAFT TORQUE CALCULATED FROM THE COMPONENT OF THE AERODYNAMIC MOMENTS IN THE PLANE OF ROTATION.

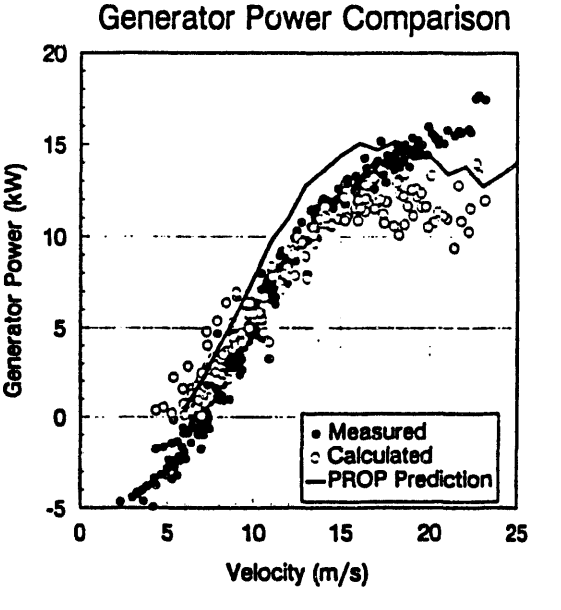

FIGURE 12: COMPARISON OF CYCLE AVERAGED GENERATOR POWER TO POWER CALCULATED FROM THE AERODYNAMIC MOMENTS. ALSO SHOWN IS THE POWER OUTPUT PREDICTED BY THE PROP CODE.

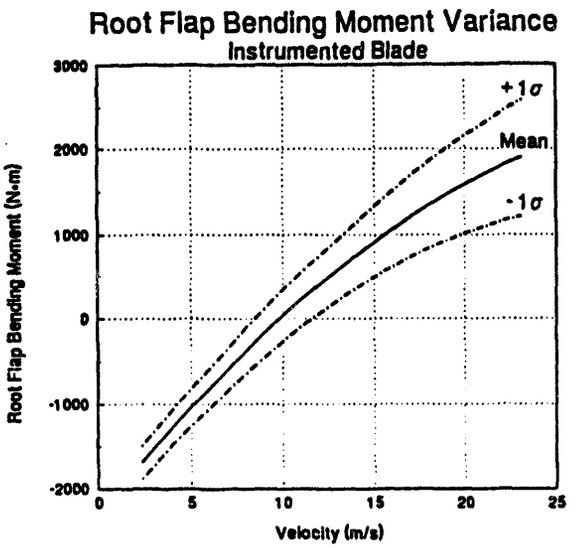

FIGURE 13: MEAN ROOT FLAP BENDING MOMENT WITH A 1σ STANDARD DEVIATION. VARIANCE INCREASES AT HIGHER VELOCITIES DUE TO AN INCREASE IN THE NUMBER OF DYNAMIC STALL EVENTS.

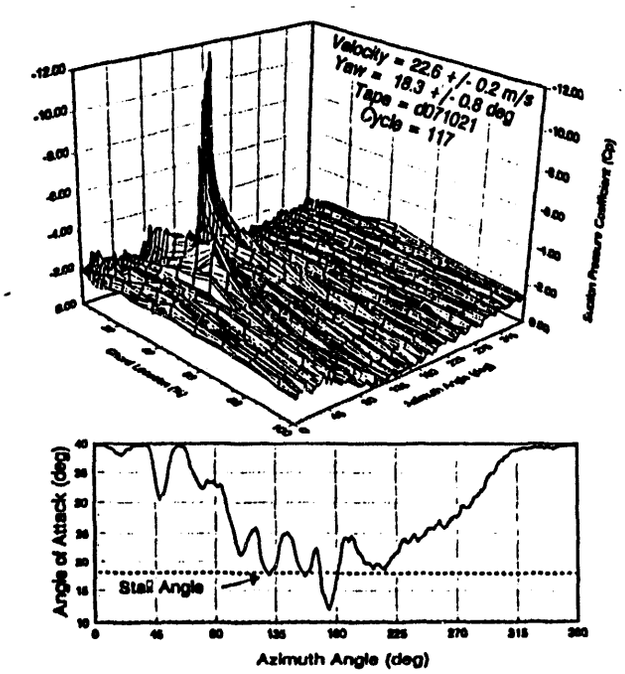

FIGURE 14: DYNAMIC STALL EVENT INDUCED BY THE COMBINATION OF YAWED FLOW AND TOWER SHADOW EFFECTS.

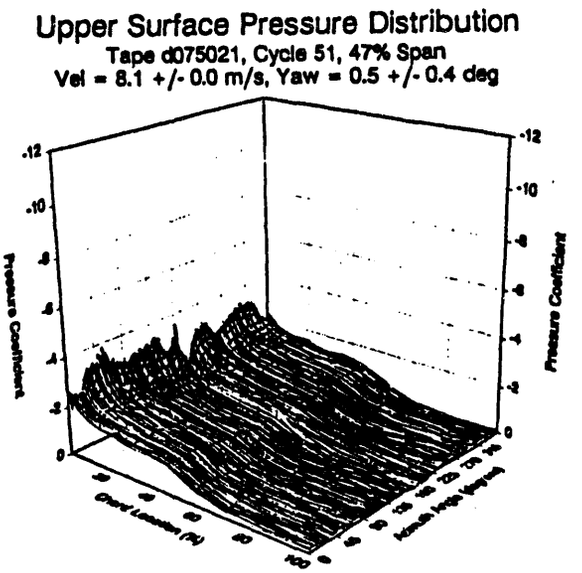

FIGURE 15: 47% SPAN UPPER SURFACE PRESSURE PROFILE FOR THE LOW VELOCITY CASE. FLOW IS ATTACHED OVER THE ENTIRE CYCLE.

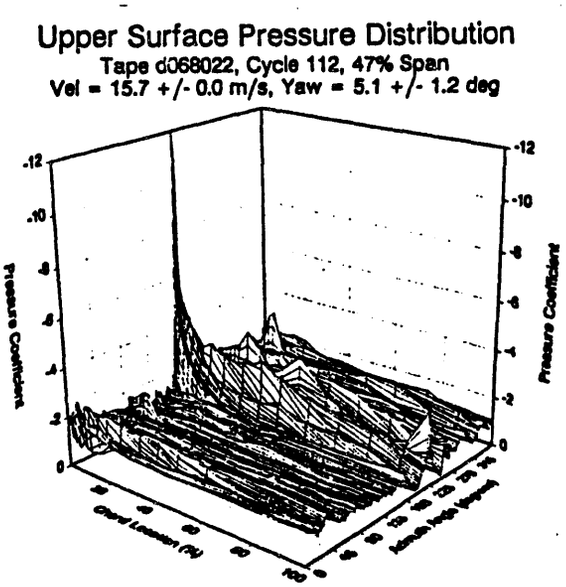

FIGURE 16: 47% SPAN UPPER SURFACE PRESSURE PROFILE FOR THE HIGH VELOCITY CASE. A LARGE, TRANSIENT PRESSURE PEAK INDICATIVE OF DYNAMIC STAL IS SEEN ON THE LEADING EDGE.

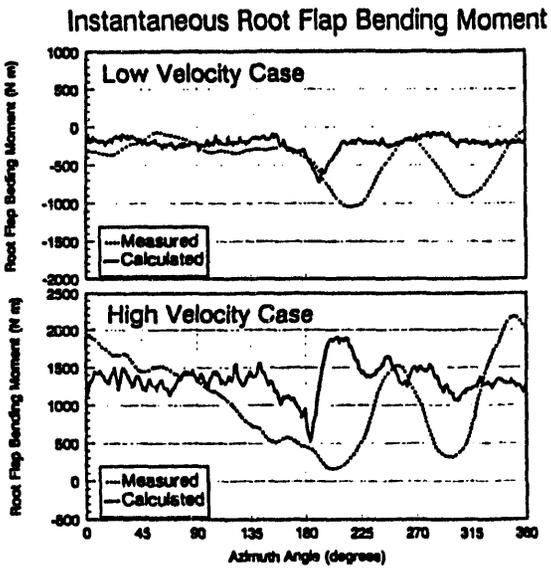

FIGURE 17: COMPARISON OF MEASURED AND CALCULATED ROOT FLAP BENDING MOMENT. MAGNITUDE OF BLADE RESONANCE INCREASES WITH THE SIZE OF APPLIED AERODYNAMIC IMPULSE.

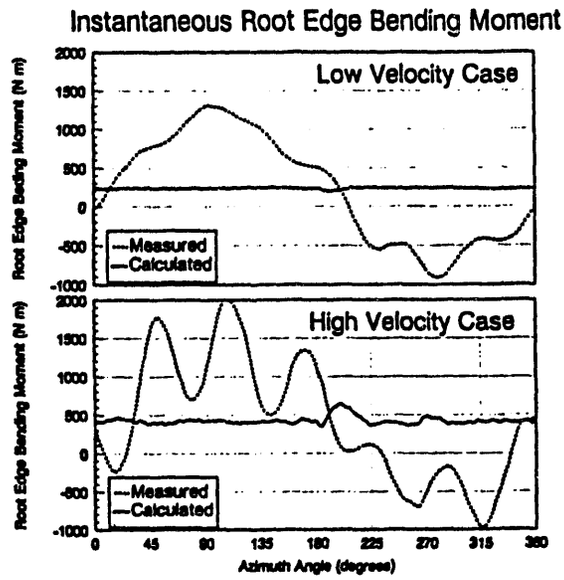

FIGURE 18: COMPARISON OF MEASURED AND CALCULATED ROOT EDGE BENDING MOMENT. GRAVITY LOADING DOMINATES, BUT BLADE RESONANCE IS AMPLIFIED BY UNSTEADY AERODYNAMIC EVENTS.

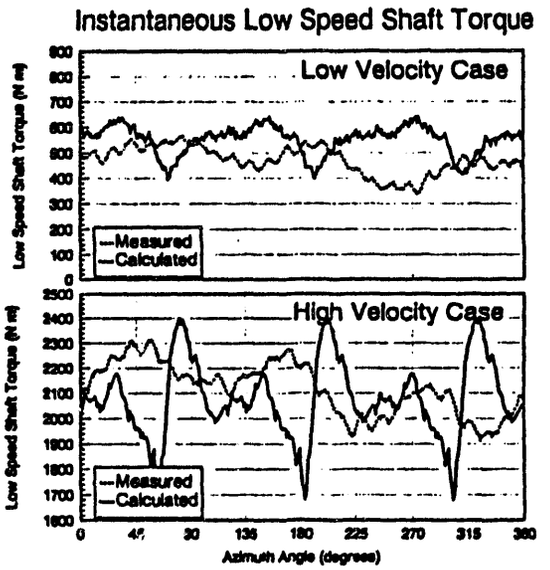

FIGURE 19: COMPARISON OF MEASURED AND CALCULATED LOW SPEED SHAFT TORQUE. SINGLE BLADE RESULT PHASE SHIFTED AND ADDED TO REFLECT CONTRIBUTION OF OTHER TWO BLADES. RESULT CORRELATES POORLY WITH MEASURED VALUES.